Phase-field-based structural optimization of 3D cross-lattice structure to lightweight periodic lattice cells

Leonie Wallat [a,b], Martin Reder[b,c], Marcus Seiler[d], Michael Selzer [e], Frank Poehler[a] and Britta Nestler[b,c,e]

[a]Institute of Materials and Processes, Karlsruhe University of Applied Sciences, Karlsruhe, Germany; [b]Institute for Applied Materials—Microstructure Modelling and Simulation, Karlsruhe Institute of Technology (KIT), Karlsruhe, Germany; [c]Institute of Digital Materials Science, Karlsruhe University of Applied Sciences, Karlsruhe, Germany; [d]ReOss GmbH, Filderstadt, Germany; [e]Institute of Nanotechnology, Karlsruhe Institute of Technology (KIT), Eggenstein-Leopoldshafen, Germany

ABSTRACT

This study explores the potential of different load-specific phase-field-based structural optimization for generating new, innovative lightweight periodic lattice structures. Initially, a three-dimensional cross-lattice structure with a volume fraction of 75% is volume-reduced to 35% by removing material from less stressed regions under various shear load scenarios. This process leads to a topological modification of the original structures. Subsequently, a phase-field-based shape optimization is applied to the structures, maintaining the volume fraction of 35%. This shape optimization aims to enhance the mechanical properties of the structures further. The investigation demonstrates that this shape optimization leads to a significant performance improvement of the structures. Comparison of the newly generated structures with established reference structures, such as the primitive and gyroid structures, highlights the potential and advantages of phase-field-based structural optimization. Notably, in the case of three-dimensional shear loading, the optimization process results in a structure with the highest shear modulus among those studied.

KEYWORDS

Structural optimization; lattice structures; phase-field; TPMS structure

1. Introduction

Especially in the current era of lightweight design and resource conservation, structural optimization and the use of cellular structures are playing an increasingly significant and important role (Ashby 2005, Tung, Wang, and Chen 2020). Structural optimization is distinguished from shape and topology optimization, among other classifications (Tang and Chang 2001). While shape optimization does not allow changes to the initial topology, such as adding holes, topology optimization permits such modifications.

Over time, various methods have been developed in the scientific community. A well-known optimization approach is the Evolutionary Structural Optimization (ESO) method, in which material is progressively removed from the structure. An extension of this method is Bi-directional Evolutionary Structural Optimization (BESO), which allows for both the removal and addition of material, enabling a more flexible and efficient optimization process (Dong *et al.* 2020, Ghabraie *et al.* 2010, Teimouri, Mahbod, and Asgari 2021, Zhao 2014). For instance, the BESO method was

used by Dong *et al.* (2020) to create hybrid structures composed of solid and lattice materials specifically designed for the additive manufacturing process. In Teimouri, Mahbod, and Asgari (2021), hybrid solid–lattice structures, consisting of various rod-based lattice frames connected to topology-optimized solid structures, were developed.

A promising, yet not widely explored, approach for structural optimization is the use of interface-based methods, such as the Phase Field Method (PFM). One advantage of this method is that it allows for the consideration of complex geometries without requiring geometry-specific discretization, such as body-fitted meshes. Owing to its physical surface kinetics, which are based on thermodynamic disequilibrium, the method results in a continuous change of the structural boundary towards a more energetically favourable state. Applications of the PFM include alloy solidification (Nestler, Garcke, and Stinner 2005) and grain growth (Moelans, Blanpain, and Wollants 2008, Steinbach 2009). It is also possible to determine the effective stiffness of stochastic foams using the PFM (Reder *et al.* 2023), which is employed in the following sections.

The promising possibilities of phase-field-based structural optimization, which are based on Allen–Cahn (Allen and Cahn 1979) approaches, have been demonstrated in various studies, such as those by Wallin and Ristinmaa (2013), Auricchio *et al.* (2020) and Xie *et al.* (2023), for optimizing different material properties. These approaches primarily focus on two-dimensional structures, with only a few studies considering three-dimensional structures (Auricchio *et al.* 2020). Furthermore, it has been demonstrated that complex porous structures can be shape-optimized using the phase field method. In Wallat *et al.* (2023), Triply Periodic Minimal Surfaces (TPMSs) were shape-optimized under specific loading conditions. In the subsequent experimental validation (Wallat *et al.* 2024), correlation between the experimental and simulation-based data was established.

In the case of targeted topology optimization using interface-based methods, adding holes is necessary to create new interfaces for structural optimization (Wang *et al.* 2024). For example, Xia, Shi, and Xia (2019) used the Bi-directional Evolutionary Structural Optimization (BESO) approach to remove material from the interior of the structure for level-set based topology optimization. This material removal is based on setting thresholds, such as defining the percentage to be removed in each iteration. The optimization process was demonstrated using 2D examples. Gao, Song, and Mao (2020) combined the BESO approach with the phase-field-based Allen–Cahn approach for structural topology optimization of 2D structures. A recent study (Wang *et al.* 2024) also introduced holes into the initial structure for targeted topology modification of a 2D structure before subsequent optimization using the phase-field-based approach.

The novelty of the present authors' approach lies in performing a load-specific topology modification followed by shape optimization on a simple three-dimensional cross-lattice structure to create a new shear-load-specific lightweight structure with periodicity in all spatial directions.

In the first part of this study, a load-specific topology modification of the cross-lattice structure is achieved through targeted volume reduction, removing material from less stressed areas. The volume fraction of the lattice structure is reduced from 75% to approximately 35% while maintaining the periodicity of the structure. Subsequently, the structure is optimized for specific loads using a modified phase-field method based on the Allen–Cahn approach, ensuring volume preservation (Nestler *et al.* 2008). This results in novel periodic lightweight unit structures designed for the corresponding load configurations. It is shown that even minimal volume redistribution can lead to improvements in mechanical properties. In particular, phase-field-based shape optimization computationally predicts novel structure variants with an increase in the effective normalized shear modulus ($\bar{G}$-modulus) of the structurally optimized units. This adjustment is especially important, as the focus of the investigated load cases is on shear loads.

Shear stress is a critical factor that significantly influences the longevity of materials and the reliability of applications across various fields. In the construction industry, the analysis of shear forces is essential; for instance, the impact of shear on reinforced concrete beams has been studied by Xue *et al.* (2023). In medicine, the examination of shear stress and its effects is crucial, as highlighted by Brindley *et al.* (2011), Yeatts and Fisher (2011) and Pires *et al.* (2022), and it is also an important

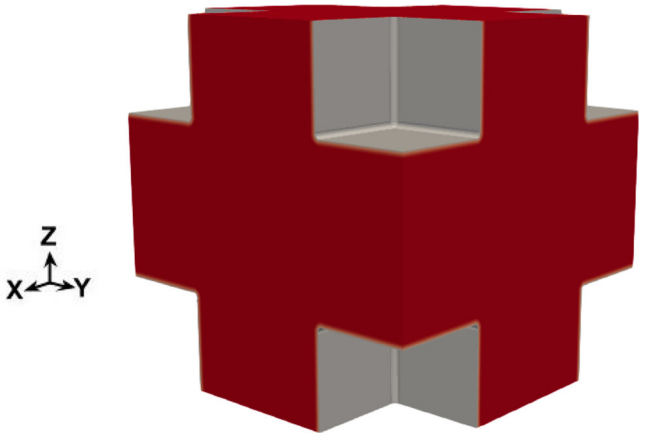

Figure 1. A periodic cross-lattice structure with a volume fraction of $\rho = 75\%$ serves as the initial structure for the optimization process.

consideration in tissue engineering (Pires *et al.* 2022, Yeatts and Fisher 2011). Pires *et al.* (2022) analysed the Wall Shear Stress (WSS) of various TPMS structures, specifically focusing on applications in the field of tissue engineering.

In the second part of the study, the newly created load-specific structures are compared with two triply periodic minimal surfaces (TPMS structures), the sheet-based gyroid and primitive structures, as well as with a lattice structure specifically designed for hydrostatic load conditions.

The findings of this study indicate that the integrated application of the load-specifically modified topology and phase-field-based shape optimization represents a promising strategy for developing highly efficient and high-performance lightweight lattice structures. These structures can be optimized further for various load orientations, and designed and tailored for specific applications where mechanical efficiency and material conservation are critical.

2. Methodology and implementation

In the following, a periodic cross-lattice structure with a volume fraction of approximately 75%, shown in Figure 1, is structure-optimized for load-specific shear cases.

Regarding the topology adjustment, the volume of the shear-loaded structures is first reduced to a volume fraction of approximately 35% through a process called *hole nucleation* (see Section 2.1). Subsequently, the volume-reduced and topology-modified structure is shape-optimized while maintaining its volume fraction.

The goal of this optimization is to achieve load-specific periodic cell structures while simultaneously increasing the shear modulus G for each load case. Both the hole nucleation process and the subsequent shape optimization are treated as a two-phase phase-field problem with a solid phase (ϕ_s) and a porous phase (ϕ_p), to which a zero stiffness is assigned. The porous phase represents the stress-free surrounding structure.

In the following, the hole nucleation process will be discussed first, followed by the phase-field-based optimization approach. This section will also provide a detailed explanation of the effective material properties and the boundary conditions used.

2.1. Hole nucleation

The first step of the optimization procedure is achieved by topology modification using a 'hole nucleation' mechanism. For the stress-specific volume reduction, material is removed from regions where

the von Mises stress, $\sigma_{\mathrm{vM}} := \sqrt{3/2}\,\|\,\mathrm{dev}(\boldsymbol{\sigma})\|$, of the loaded initial lattice structure falls below a certain percentage value ρ_{nuc} of its maximum value. The corresponding nucleation criterion at a point $\boldsymbol{x}$ reads

$$\sigma_{\mathrm{vM}}(\boldsymbol{x}) < \rho_{\mathrm{nuc}} \max_{\Omega}(\sigma_{\mathrm{vM}}) \tag{1}$$

with $\max(\sigma_{\mathrm{vM}})$ being the maximum value of the von Mises stress in the domain Ω and ρ_{nuc} the threshold ratio to start nucleation. The von Mises stress field $\sigma_{\mathrm{vM}}(\boldsymbol{x})$ is determined by linear elastic simulations to mechanical equilibrium under the given loading conditions. To this end, the initial structure is discretized using a Cartesian grid and the stationary momentum balance (5) is solved. Details may be found in Section 2.2, where the same simulation approach for the elasticity is embedded in the shape optimization process. Thus, in cells of the computational grid where the von Mises stress is below the threshold value $\rho_{\mathrm{nuc}} \max(\sigma_{\mathrm{vM}})$, the porous phase is assigned by setting the phase-field values $\phi_{\mathrm{p}} = 1$ and $\phi_{\mathrm{s}} = 0$. This leads to a decrease in the solid volume V_{s}, which is implicitly determined by the choice of the threshold value ρ_{nuc}. Since this volume reduction is stress-specific, an individual value of ρ_{nuc} needs to be chosen for each load case to reach a specific target volume fraction $c_{\mathrm{s}} = V_{\mathrm{s}}/V$. Subsequently, a target value of 35%, and thus a porosity of 65%, is chosen. The threshold ρ_{nuc} is iteratively determined by solving for the condition $c_{\mathrm{s}}(\rho_{\mathrm{nuc}}) - 0.35 = 0$ by using the method of nested intervals. Alternatively, the value of ρ_{nuc} could be incrementally increased until the desired volume fraction is reached, yielding a similar approach to evolutionary structural optimization, which would lead to a more robust optimization process. However, since the topology adjustment step is succeeded by a shape optimization, the accuracy of the first step is less important, and thus the computationally cheaper approach with nested intervals is employed.

After the original lattice structures are stress-specifically topology-optimized, phase-field-based shape optimization is performed under volume preservation. This consistent volume fraction of the structures allows for better comparison of the optimized structures.

2.2. Phase-field based optimization approach

For the structural optimization, a modified phase-field approach is utilized. The approach used here is based on the Allen–Cahn method (Allen and Cahn 1979), which incorporates a volume preservation constraint for the considered phases (Nestler *et al.* 2008). The evolution of the phase field is derived from the minimization of a Ginzburg–Landau free energy density functional, which depends on the phase-field tuple and the corresponding gradients (Garcke, Nestler, and Stoth 1999).

Generally, the free energy functional $\mathcal{F}(\phi, \nabla\phi) = \mathcal{F}_{\mathrm{int}}(\phi, \nabla\phi) + \mathcal{F}_{\mathrm{bulk}}(\phi, \dots)$ is divided into an interfacial contribution $\mathcal{F}_{\mathrm{int}}(\phi, \nabla\phi)$ (Daubner *et al.* 2023) and a bulk region contribution $\mathcal{F}_{\mathrm{bulk}}(\phi, \dots)$ (Daubner *et al.* 2023, Equation (1)).

As described in the following, $\mathcal{F}_{\mathrm{bulk}}$ arises from the mechanical strain energy and is therefore expressed as follows:

$$\mathcal{F}_{\mathrm{bulk}} = \mathcal{F}_{\mathrm{el}}(\phi, \boldsymbol{u}) = \int_{\Omega} f_{\mathrm{el}}(\phi, \vec{\boldsymbol{u}})\,\mathrm{d}V = V\bar{f}_{\mathrm{el}}(\phi, \vec{\boldsymbol{u}}). \tag{2}$$

The interfacial contribution is expressed as

$$\mathcal{F}_{\mathrm{int}}(\phi, \boldsymbol{u}) = \int_{\Omega} f_{\mathrm{grad}}(\phi, \nabla\phi) + f_{\mathrm{pot}}(\phi)\,\mathrm{d}V \tag{3}$$

comprising a gradient energy density f_{grad} and a potential energy f_{pot}. The volume preservation is ensured by the Lagrange multiplier λ_{vol} (*cf.* Nestler *et al.* 2008). Combining both contributions in Equations (2) and (3), an additional positive contribution $\mathcal{F}_{\mathrm{Vol}}(\phi)$ is incorporated, which ensures the

volume preservation (see Nestler *et al.* 2008); the energy functional for the subsequent analysis is given by

$$\mathcal{F}(\phi, \boldsymbol{u}) = \mathcal{F}_{\text{int}}(\phi, \nabla\phi) + \mathcal{F}_{\text{el}}(\phi, \boldsymbol{u}) + \mathcal{F}_{\text{Vol}}(\phi). \tag{4}$$

The optimization is achieved using the phase-field evolution equation yielded by the volume preserving Allen–Cahn approach with an obstacle potential. From variational derivation, the stationary momentum balance and the Allen–Cahn equation are obtained, reading

$$\nabla \cdot (\boldsymbol{\sigma}) = 0, \tag{5}$$

$$\frac{\partial \phi_{\text{s}}}{\partial t} = \frac{M}{\epsilon}\left[2\gamma\,\epsilon(\Delta\phi_{\text{s}} - \|\nabla\phi_{\text{s}}\|\nabla\cdot\boldsymbol{n}) - \frac{16\gamma}{\pi^2\epsilon}(1-2\phi_{\text{s}}) - \lambda_{\text{vol}} + \frac{\partial h(\phi_{\text{s}})}{\partial\phi_{\text{s}}} f_{\text{el}}\right], \tag{6}$$

with the stress $\boldsymbol{\sigma} = h(\phi_{\text{s}})\mathbb{C}_{\text{s}}[\boldsymbol{\epsilon}]$ and strain energy density $f_{\text{el}} = \frac{1}{2}\mathbb{C}_{\text{s}}[\boldsymbol{\epsilon}]\cdot\boldsymbol{\epsilon}$. Here, ϵ determines the width of the diffuse interface and γ the surface tension. Additionally, M is a mobility coefficient. Furthermore, the curvature-minimizing dynamics of the Allen–Cahn equation are eliminated by the term $\|\nabla\phi_{\text{s}}\|\nabla\cdot\boldsymbol{n}$ with $\boldsymbol{n} := \nabla\phi_{\text{s}}/\|\nabla\phi_{\text{s}}\|$ (Schoof *et al.* 2018, Sun and Beckermann 2007). As a result, the interface terms proportional to γ only cause relaxation toward the phase-field equilibrium profile while maintaining the actual geometry, which corresponds to the isosurface where $\phi_{\text{s}} = 0.5$. Therefore, within the context of this work, the surface tension γ does not represent a physical parameter.

For the optimization problem, a two-phase problem is addressed. This involves distinguishing between a solid phase (ϕ_{s}) and a porous phase (ϕ_{p}), which exhibits no stiffness. An average stress $\bar{\boldsymbol{\sigma}}$ is used, which should fulfil the following condition in addition to periodicity:

$$\bar{\boldsymbol{\sigma}} = \frac{1}{\Omega}\int_{\Omega} \sigma\,(\phi_{\text{s}}, \boldsymbol{u}(\phi_{\text{s}}))\,\mathrm{d}V. \tag{7}$$

The approach involves generating the average stress by selecting the average strain via displacement boundary conditions in an iterative procedure, so that the elastic energy contribution $\tilde{\mathcal{F}}_{\text{strain}}$ is selected as the driving force. For a given strain $\boldsymbol{\epsilon}^{(n)}$ at iteration step n, the elastic equilibrium is solved and then updated to the next iteration step $(n+1)$ according to

$$\bar{\boldsymbol{\epsilon}}^{(n+1)} = \bar{\boldsymbol{\epsilon}}^{(n)} + \bar{\mathbb{C}}^{-1}(\phi_{\text{s}})\cdot\left(\bar{\boldsymbol{\sigma}} - \frac{1}{\Omega}\int_{\Omega}\boldsymbol{\sigma}(\phi_{\text{s}}, \boldsymbol{u}^{(n+1)})\,\mathrm{d}V\right) \tag{8}$$

with the fourth-order averaged stiffness tensor $\bar{\mathbb{C}} = \int \mathbb{C}_{\text{s}}\phi_{\text{s}}\,\mathrm{d}V$. The initial strain $\boldsymbol{\epsilon}^{(0)} = (\bar{\mathbb{C}}(\phi_{\text{s}}))^{-1}\bar{\boldsymbol{\sigma}}$ is used.

To account for the new dependencies, the displacement field is decomposed into $\tilde{\boldsymbol{u}}$ and $\bar{\boldsymbol{\epsilon}}\cdot x$. This introduces an additional dependency of the functional on $\bar{\boldsymbol{\epsilon}}$ with respect to $\boldsymbol{\phi}$, *i.e.* $\tilde{\mathcal{F}}_{\text{el}}(\phi_{\text{s}}, \tilde{\boldsymbol{u}}(\phi_{\text{s}}), \bar{\boldsymbol{\epsilon}}(\boldsymbol{\phi}))$. Consequently, the free energy functional is given by

$$\mathcal{F}(\phi_{\text{s}}) = \mathcal{F}_{\text{int}}(\phi_{\text{s}}) + \tilde{\mathcal{F}}_{\text{el}}\big(\phi_{\text{s}}, \tilde{\boldsymbol{u}}(\phi_{\text{s}}), \bar{\boldsymbol{\epsilon}}(\phi_{\text{s}})\big) + \mathcal{F}_{\text{vol}} \tag{9}$$

with the elastic free energy

$$\tilde{\mathcal{F}}_{\text{el}}\big(\phi_{\text{s}}, \tilde{\boldsymbol{u}}(\phi_{\text{s}}), \bar{\boldsymbol{\epsilon}}(\phi_{\text{s}})\big) = \int_{\Omega}\frac{1}{2}\mathbb{C}(\phi_{\text{s}})\big[\boldsymbol{\epsilon}\big(\tilde{\boldsymbol{u}}(\phi_{\text{s}})\big) + \bar{\boldsymbol{\epsilon}}(\phi_{\text{s}})\big]\cdot\big[\boldsymbol{\epsilon}\big(\tilde{\boldsymbol{u}}(\phi_{\text{s}})\big) + \bar{\boldsymbol{\epsilon}}(\phi_{\text{s}})\big]\,\mathrm{d}V, \tag{10}$$

since the shape optimization is conducted under volume preservation, allowing for a more accurate comparison between the initial and optimized structures.

2.3. Simulation software

For structure generation, for the process of volume reduction through nucleation, as well as for the subsequent shape optimization, the in-house simulation software 'Parallel Algorithms for Crystal Evolution in 3D' (Pace3D) is used (Hötzer *et al.* 2018). This framework enables structural–mechanical simulations for given load scenarios, where the geometry interface is varied to minimize the stored elastic energy. Additionally, the software includes various functions that enable, for example, the verification and output of the current volume.

2.4. Simulation setup and material properties

The cross-lattice structure to be optimized is considered in a three-dimensional domain Ω with 200 cells in each spatial direction. The parameters used in the conducted optimization follow the use of $\epsilon = 0.015L$, which corresponds to an interface width of approximately $0.0375L$, considering the edge length $L = 1\,\mathrm{m}$ of the domain. This allows for a resolution of the diffuse interface with seven cells. Furthermore, the parameters chosen are $\gamma = 0.02\,\mathrm{kg\,s^{-2}}$, the mobility parameter $M = 1.0\,\mathrm{m^2\,s\,kg^{-1}}$ and the timestep size $\Delta t = 1.75 \times 10^{-4}\,\mathrm{s}$.

The simulation is conducted within the linear elastic range. Additionally, isotropic materials are assumed in the simulation process following the constitutive equation

$$\boldsymbol{\sigma} = \mathrm{dev}(\boldsymbol{\sigma}) + \mathrm{sph}(\boldsymbol{\sigma}) = 2G\,\mathrm{dev}(\boldsymbol{\epsilon}) + 3K\,\mathrm{sph}(\boldsymbol{\epsilon}) \tag{11}$$

with $\mathrm{sph}(\cdot) := 1/3\ \mathrm{trace}(\cdot)\mathbf{1}$ and $\mathrm{dev}(\cdot) := (\cdot) - \mathrm{sph}(\cdot)$ being the spherical and deviatoric part of a second-order tensor. Furthermore, G and K denote the shear and bulk moduli, respectively, which are sufficient to determine the stiffness tensor $\mathbb{C}$ in the isotropic case, *cf. e.g.* Reder *et al.* (2023, Equation (9)).

3. Results and discussion

The initial cross-lattice structure, with a volume fraction of 75%, is subjected to volume reduction under specific shear load criteria. Material is removed from the less-loaded regions, so that the resulting structure achieves a volume fraction of approximately 35%. Since the structures are subjected to pure shear loading, the aim of the present work is to maximize the effective shear modulus of structures under the given load conditions. After that, a shape optimization of the topology-modified structure takes place.

3.1. Structure optimization under shear loading scenarios

3.1.1. Considered loading scenarios

The cross-lattice structure is subjected to three cases of unidirectional and multidirectional shear loads, defined by the stress tensors in Equation (12), and volume reduction is performed according to the loading scenarios. A stress of $\sigma = -7$ is applied in each respective loading direction.

$$\bar{\sigma}_{\mathrm{case1}} = \begin{bmatrix} 0 & -\sigma & 0 \\ -\sigma & 0 & 0 \\ 0 & 0 & 0 \end{bmatrix}, \quad \bar{\sigma}_{\mathrm{case2}} = \begin{bmatrix} 0 & -\sigma & -\sigma \\ -\sigma & 0 & 0 \\ -\sigma & 0 & 0 \end{bmatrix}, \quad \bar{\sigma}_{\mathrm{case3}} = \begin{bmatrix} 0 & -\sigma & -\sigma \\ -\sigma & 0 & -\sigma \\ -\sigma & -\sigma & 0 \end{bmatrix}. \tag{12}$$

For volume reduction, material is removed from the cross-lattice structure at less stressed areas according to the three considered loading criteria. The resulting structures are depicted from various perspectives in Figure 2.

The volume reduction step leads to periodic and symmetrical structures for the three considered load cases. It is evident that the volume is reduced according to the loading orientation. As can be

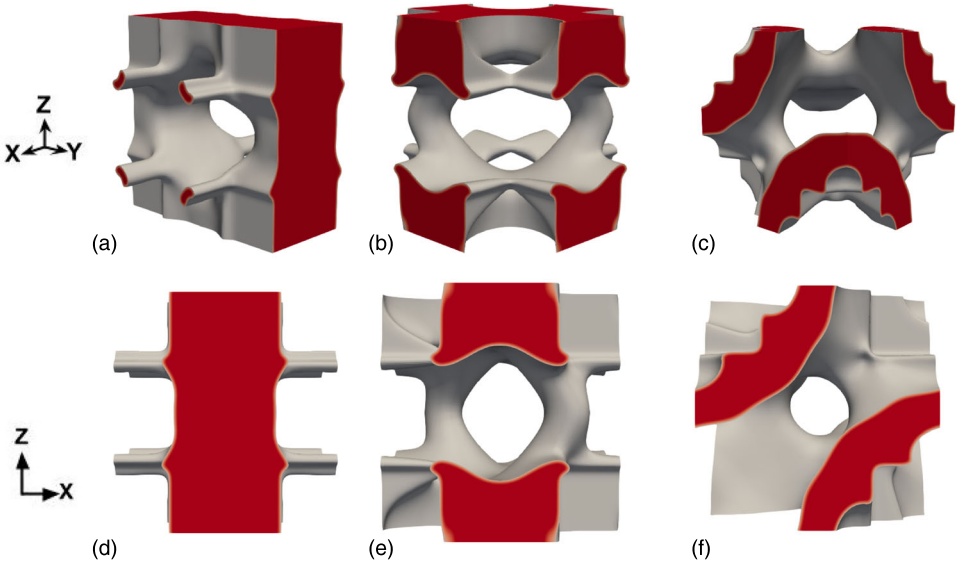

Figure 2. Volume-reduced and topologically modified cross-structure under different shear loading criteria (*xyz*- and *xz*-views). (a) Case 1: Unidirectional shear loading in the *x*-direction. (b) Case 2: Multidirectional shear loading in the *x*- and *y*-directions. (c) Case 3: Multidirectional shear loading in the *x*-, *y*- and *z*-directions. (d) Case 1: Unidirectional shear loading in the *x*-direction. (e) Case 2: Multidirectional shear loading in the *x*- and *y*-directions and (f) Case 3: Multidirectional shear loading in the *x*-, *y*- and *z*-directions.

Table 1. Volume fraction of the porous structures and their corresponding surface areas.

Modified structure type	Volume fraction	Surface area
Unidirectional	0.36	2.77
Bidirectional	0.36	3.54
Tridirectional	0.36	3.70

seen from the topology-modified structure under the shear loading conditions of case 1, a more pronounced anisotropic geometry is present and remains at a later stage. In contrast, the muldirectional shear loading case 3 results in a curved lattice structure that bears certain similarities to triply periodic minimal surfaces. The structure in case 2 can be identified as an intermediate structure between case 1 and case 3.

These observations highlight the strong dependence of the geometry of the porous structures on the specific loading orientation. In unidirectional loading applications as case 1, where the load is applied in a single direction, the structures tend to develop anisotropic material behaviour. This occurs because material is primarily removed from areas not exposed to the main loading direction, leading to an uneven distribution of porosity. In contrast, three-dimensional loading as in case 3, where the load is applied simultaneously in multiple directions, results in a more uniform and symmetric pore structure. These structures often resemble triply periodic minimal surfaces structures, known for their beneficial mechanical properties and even material distribution.

Loading case 2, representing a combination of unidirectional and multidirectional loading, results in an intermediate structure. This structure exhibits characteristics of both the unidirectional and three-dimensional loading cases, providing insights into the transitional mechanisms between different loading scenarios.

All structures have a volume fraction of 36%. The corresponding initial surface areas of the structures are computationally determined and listed in Table 1.

The modified structure type ‘unidirectional’ represents the unidirectionally load-modified structure, which is shown in Figure 2(a). Similarly, ‘bidirectional’ corresponds to the bidirectionally

Table 2. Behaviour of the normalized effective shear modulus $\bar{G}$ of load-modified cross-lattice structures under different loading conditions, and the average of all three cases.

	Shear type			
Modified structure type	Unidirectional	Bidirectional	Tridirectional	Average
Unidirectional	0.19	0.0098	0.0085	0.069
Bidirectional	0.05	0.06	0.07	0.06
Tridirectional	0.1	0.13	0.22	0.15

load-modified structure (see Figure 2(b)), and 'tridirectional' describes the modified structure subjected to loading in all directions (see Figure 2(c)). This labelling will be consistently maintained throughout the following sections.

While the volume fraction of the three structures remains constant, there is a significant difference in the surface area. The resulting porous structure from the unidirectional loading case has the smallest surface area. In contrast, the structure subjected to shear loading from all directions shows an approximately 33% larger surface area. The value of the surface area determined for case 2 lies between the other two cases.

Following Reder *et al.* (2023), the subsequent results are given in normalized manner. Thereby, the effective shear modulus is subsequently normalized by its Voigt bound, which represents an upper limit for the effective stiffness in composite materials (Voigt 1889). It is given by the arithmetic mean of the shear moduli of the involved phases with respect to the corresponding volume fraction, and thus, since the pore has zero stiffness, by $G_V = G_s c_s$. Herein, the shear modulus of the solid is $G_s = 5480$ MPa and the solid volume fraction $c_s = 0.35$. Therefore, the normalized effective shear modulus is $\bar{G} = \bar{G}^*/(G_s c_s)$, with $\bar{G}^*$ being the effective shear modulus.

Table 2 lists the normalized effective shear modulus $\bar{G}$ of the structures for the respective loading cases and their average, $\bar{G}_{Av}$. Thereby, the modified structure types of the specific loading cases are subjected to all three loads (Uni-, bi- and tri-directional) to investigate the influence of the modification regarding one load case on the effective stiffness for other load cases. The adjusted structures for case 1 and case 3 exhibit the highest $\bar{G}$ of 0.19 [−] (case 1, unidirectional) and 0.22 [−] (case 3, tridirectional) for their respective loading conditions compared to the other structures.

The orientation of the volume in response to the specific loading scenario is most clearly demonstrated by case 1. For the adjusted loading case, the normalized effective shear modulus $\bar{G}$ is 0.19 [−] (case 1, unidirectional), whereas it is significantly lower for the multidirectional loading cases, with values of 0.0098 [−] (case 1, bidirectional) and 0.0085 [−] (case 1, tridirectional). Interestingly, the structure modified for the two-dimensional shear loading case exhibits a higher modulus for the three-dimensional case of $\bar{G} = 0.07$ than for the optimized two-dimensional shear loading case of $\bar{G} = 0.06$. Among the structures analysed, the structure modified for case 2 exhibits the smallest deviations in the normalized effective shear modulus $\bar{G}$ across the various load cases considered. This suggests that this structure demonstrates the best isotropic behaviour, as it provides the most uniform mechanical response under different loading scenarios.

The structure from case 3 with shear moduli of $\bar{G} = 0.1, 0.13, 0.22$ shows the best performance over all three loading scenarios. It still has a relatively high shear modulus for the loads for which it was not modified, and a normalized effective shear modulus approximately twice as high in case 3, it was not modified for and an approximately double as high normalized effective shear modulus in case 3. This observation is confirmed by the average value ($\bar{G}_{Av}$) across all three loading cases. Overall, the structure modified for case 3 shows the highest mean value. Although the shear modulus for case 1 is relatively high in the modified loading direction, the values in the other loading directions are significantly lower, which explains the correspondingly lower average value.

In the following subsection, the topologically adapted structures will be optimized for the respective modified loading directions.

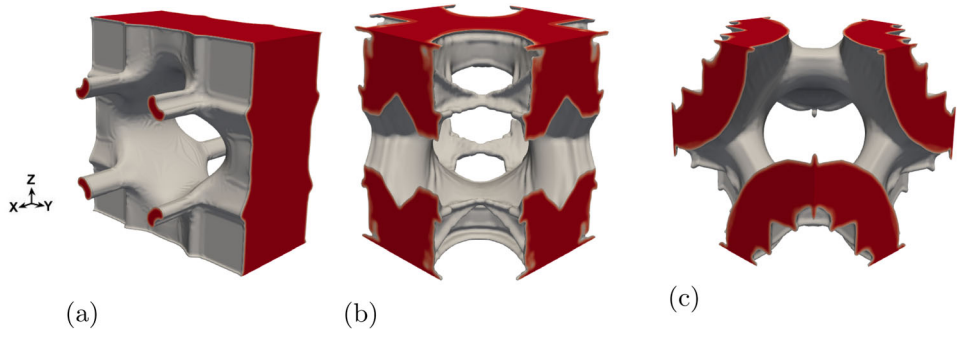

Figure 3. Shape optimization of topologically modified cross-structure under different shear loading criteria (*xyz*-view). (a) Case 1: Unidirectional shear loading in the *x*-direction. (b) Case 2: Multidirectional shear loading in the *x*- and *y*-directions and (c) Case 3: Multidirectional shear loading in the *x*-, *y*- and *z*-directions.

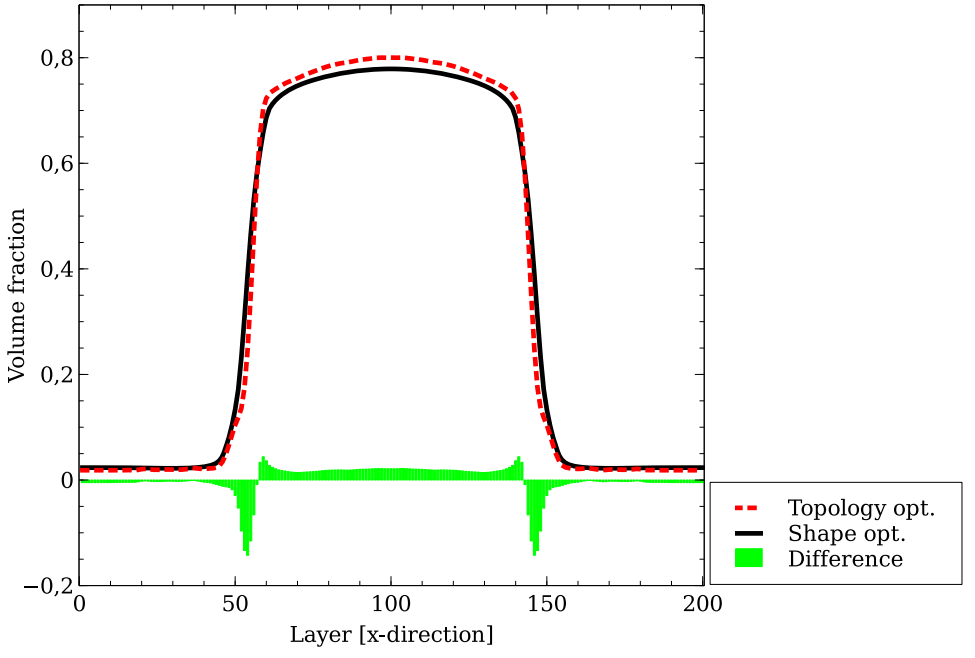

Figure 4. Volume redistribution through the shape optimization process of the optimized structure for case 1.

3.1.2. Shape optimization

The previously topology-altered structures are now shape-optimized under specific shear loading conditions. The shape optimization process is terminated once the change in the objective function after each simulation step is reduced to less than the fifth decimal place after the decimal point.

The phase-field-based shape optimization process aims to optimize the structures further according to the respective loading directions. During this process, the volumes of the structure keep constant while redistributing the volume. Volume is removed from less-loaded regions and added to more heavily loaded areas. Nevertheless, the structure's periodicity is maintained. In Figure 3, the shape-optimized cell structures are shown in their shape-optimized state.

Since the volume redistribution is not fully recognizable in Figure 3, the volume fraction along the *x*-axis of the respective structures is presented in more detail in the following Figures 4, 5 and 6.

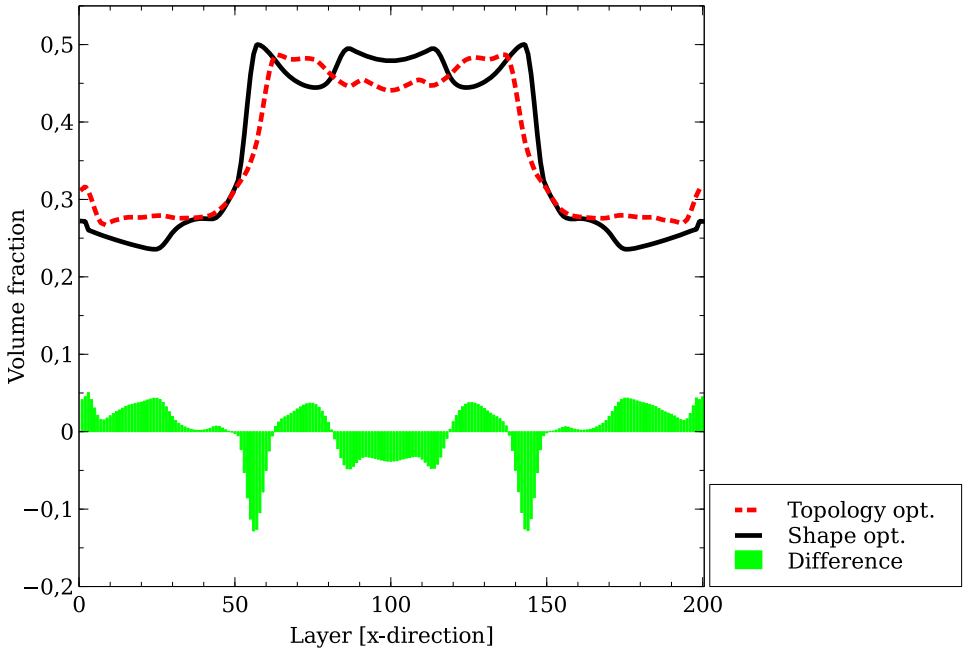

Figure 5. Volume redistribution through the shape optimization process of the optimized structure for case 2.

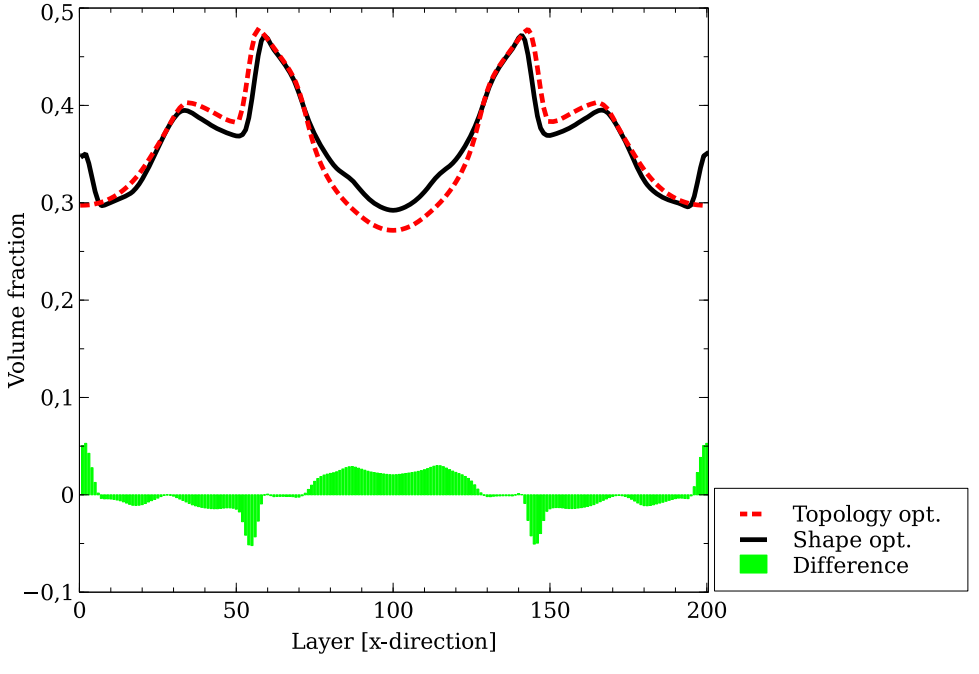

Figure 6. Volume redistribution through the shape optimization process of the optimized structure for case 3.

This detailed representation allows for a more precise analysis of the volume distribution within the structures, which has corresponding impacts on the mechanical properties of the structures.

The red dashed lines in Figures 4, 5 and 6 represent the initial topology-adjusted structure, while the subsequent shape-optimized structure is indicated by solid black lines. The difference in volume

Table 3. Volume fraction of the shape optimized porous structures, as well as their corresponding surface areas.

Shape modified structure type	Volume fraction	Surface area
Unidirectional	0.36	3.01
Bidirectional	0.36	4.33
Tridirectional	0.36	3.96

Table 4. Behaviour of the normalized shear modulus $\bar{G}$ of the load-altered and subsequently shape-optimized cross-lattice structures under various loading conditions and the average of all three cases.

	Shear type			
Shape modified structure type	Unidirectional	Bidirectional	Tridirectional	Average
Case 1 (unidirectional)	0.22	0.008	0.007	0.078
Case 2 (bidirectional)	0.07	0.22	0.09	0.126
Case 3 (tridirectional)	0.11	0.14	0.26	0.17

redistribution is illustrated by the bar chart. It is evident that, for the structure-optimized one-dimensional shear loading case (case 1), the volume redistribution due to the optimization process is minimal, whereas the most significant redistribution is observed in case 2. This also explains why the largest percentage change in surface area of about 22% from the initial 3.54 (see Table 1) to 4.33 (see Table 3), is observed in this case. This table also reveals that the shape-optimized structure for case 2 has the largest surface among the three structures considered.

Upon revisiting the normalized G-modulus from Table 2 for the topologically altered structures, it is evident that the topologically altered structure in case 3 exhibits a higher normalized G-modulus for the loading scenario in case 2 than the structure specifically optimized for this loading case. The subsequent shape optimization process enabled all structures to be brought into a more energetically favourable state. Consequently, after the shape optimization process, all three structures represent the most favourable design for their respective optimized loading conditions. The corresponding G-modulus for each of the shape-optimized structures and their corresponding loading conditions can be found in Table 4.

Although the volume redistribution is partly relatively minor, an increase in the shear modulus $\bar{G}$ was achieved compared to the topologically altered structure for the respective optimized loading case.

In the structure-optimized unidirectional loading scenario (case 1), the volume redistribution leads to an increase in the $\bar{G}$-modulus, from 0.19 [−] (see Table 2; case 1, unidirectional) to 0.22 [−] (see Table 4; case 1, unidirectional), representing an approximate 15% increase in the direction of optimization. However, this also results in a decrease in the effective shear modulus for multidirectional loading orientations. In contrast, for the other two structures, the volume redistribution results in an enhancement of the shear modulus across all considered shear loading scenarios compared to the load-specific topologically altered baseline structure.

The highest increase was observed in case 2, where the volume redistribution leads to an increase in the shear modulus of more than 200%.

In the structure-optimized unidirectional loading scenario (case 1), the volume redistribution leads, on one hand, to an increase in the $\bar{G}$-modulus, but on the other hand, also results in a decrease in the effective shear modulus for multidirectional loading orientations. In contrast, for the other two structures, the volume redistribution results in an enhancement of the shear modulus across all considered shear loading scenarios compared to the load-specific topologically altered baseline structure.

The highest increase was observed in case 2, where the volume redistribution leads to an increase in the shear modulus of more than 200%.

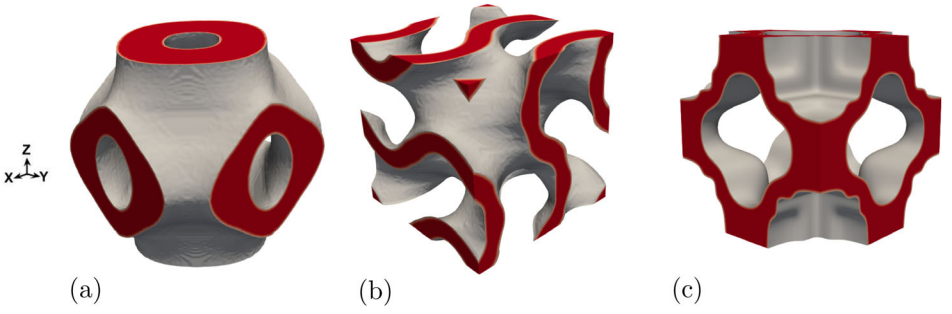

Figure 7. Comparison structures with a volume fraction of about 35%. (a) Primitive structure. (b) Gyroid structure and (c) Loading case: hydrostatic loading scenario.

In case 3, shape optimization achieved an additional increase in the modulus of approximately 18% in the direction of the applied load. As can be seen from the average value, the shape-optimized structure for loading case 3 still demonstrates the overall most beneficial behaviour across the considered load cases.

From these observations, it can be concluded that topology modification is a promising tool for developing new, load-specific foundational structures. The subsequent shape optimization process serves, depending on the efficiency of the previously determined topology, either for fine-tuning in the specific loading case or for further optimization of the structure. In addition, in the cases considered, shape optimization results in an increase in the surface area, although the surface area is not part of the optimization process.

Besides the optimized lattice structures for pure shear loading cases, it is also important to analyse comparative structures for the previously considered loading scenarios. This allows for a comprehensive assessment of the performance and efficiency of the load-specific, newly generated lattice structures through the relatively unexplored phase-field-based structural optimization for lattice structures.

3.2. Comparative structures

For comparison of the newly generated periodic structures, which were specifically optimized for various shear loading conditions, two Triply Periodic Minimal Surfaces (TPMS) are selected: the sheet-based 'gyroid' (see Figure 7(a)) and the sheet-based 'primitive' structure (see Figure 7(b)). This selection is based on the observed similarity of the optimized structure with the minimal surfaces case 3. Additionally, a structure derived from the topology-changed cross-lattice structure, but optimized for the hydrostatic loading case (see Figure 7(c)), is included in the analysis. This structure also exhibits similarities to triply periodic minimal surface structures. The finding that optimization under uniform loading conditions results in TPMS-like structures is supported by the results of Takezawa *et al.* (2018). In this study, a hollow tetrahedral cell structure is optimized with respect to its isotropic effective stiffness, further confirming the similarity of the resulting structure to TPMS structures.

All three structures have a volume fraction of about 35%, similar to the previously generated structures. However, the surface areas of these three structures are higher than those of the structures specifically optimized for shear loading cases, as can be seen from Table 5, with the gyroid structure having the largest surface area of 6.16.

The normalized effective $\bar{G}$-moduli of the comparison structures for the unidirectional and multidirectional shear loading cases applied to the cross-lattice structure are listed in Table 6.

In the mechanical analysis of the shear modulus $\bar{G}$ of the comparative structures, it is observed that the primitive structure exhibits the highest values under both, unidirectional and multidirectional shear loads compared to the other two examined structures. However, when comparing the primitive

Table 5. Volume fractions of the porous comparison structures, as well as their respective surface areas.

Comparison structure	Volume fraction	Surface area
Primitive	0.34	4.60
Gyroid	0.34	6.16
Hydrostatic	0.34	4.42

Table 6. Normalized effective shear modulus $\bar{G}$ of comparison structures and the average of all three cases.

	Shear type			
Comparison structure	Unidirectional	Bidirectional	Tridirectional	Average
Primitive	0.22	0.22	0.21	0.21
Gyroid	0.17	0.17	0.17	0.17
Hydrostatic	0.15	0.15	0.15	0.15

structure with the newly generated structures, it becomes evident that the $\bar{G}$-moduli for the newly generated structures in load cases 1 and 2 are in a similar range. This indicates that the new structures perform comparably to the primitive structure in these load cases and the mechanical properties compete well with already established structures.

Notably, the newly generated and shape-optimized structure for the three-dimensional loading scenario (case 3) can exhibit an effective $\bar{G}$-modulus that is up to 23% higher. This shows that the targeted optimization for a specific loading case can achieve the desired stiffness. However, it must be noted that the shear modulus for other loading cases of the modified structure in case 3 is nearly halved. Nevertheless, if only the specified loading case is of relevance, this load-specific optimization may still prove advantageous.

When examining the other comparative structures, the gyroid and hydrostatically modified structures have no detected significant fluctuations in the $\bar{G}$-moduli across the different loading cases. Although the structure-optimized case 3 also features a uniformly periodic arrangement, the effective $\bar{G}$-modulus has nearly halved between the optimized loading case (case 3) and the non-optimized loading cases.

To sum up, the phase-field-based load-specific optimization enables the generation and optimization of new structures. The superior performance of this newly generated structure under multidimensional loading conditions underscores the potential of phase-field-based optimization for developing more efficient structures with improved mechanical performance. While the initial load-specific topology modification creates the base structure, the subsequent shape optimization process refines the structure.

This highlights the potential of the structural optimization process using phase-field-based optimization and demonstrates the capability of computationally developing new, load-specifically designed structures. In particular, it underscores the ability of phase-field-based optimization to create structures tailored to specific loading requirements.

4. Conclusion

In the first part of this study, a three-dimensional lattice cross-structure with a volume fraction of about 75% is both topology-modified and shape-optimized for various shear loading cases. Initially, material is removed from the less-stressed areas of the original structure under unidirectional and multidirectional shear loads, resulting in a new, periodic, and topologically altered structure with a volume fraction of approximately 35%. Analysis of the shear modulus for the different loading directions reveals that the shear modulus is not optimally aligned for some structures. The subsequent phase-field-based shape optimization process leads to a stress-specific volume redistribution, resulting in an increased shear modulus for each structure tailored to its respective loading case.

In the second part of the study, two well-established triply periodic minimal surface structures from the scientific literature, namely the sheet-based gyroid and the primitive structure, and in addition a hydrostatically topology-altered lattice cross-structure, are used as comparative structures. It is observed that the primitive structure exhibits the highest shear modulus the one-dimensional and two-dimensional shear loading cases. In contrast, the shape- and topology-optimized structure achieves the highest shear modulus under three-dimensional shear loading conditions.

These results highlight that the combination of phase-field-based topology and shape optimization represents a promising approach for creating new mechanical periodic structures tailored to specific loading conditions.

The study effectively demonstrates the approach, concept and potential for generating stress-specific periodic porous structures using a phase-field-based structural optimization process.

Since the computational costs for shape optimization are high owing to the numerous iterations, which is not the case for topology modification owing to the single-step process, future work will also focus on improving computational efficiency and optimization. One way to reduce these costs is by optimizing the mechanical solver. Additionally, another research field is to extend these methods to consider *e.g.* manufacturing restrictions, multiphase materials or dynamic lead influences. Furthermore, the framework will be applied to other structural types and different mechanical requirements, aiming to develop new lightweight structures for industrial applications.

Disclosure statement

No potential conflict of interest was reported by the author(s).

Funding

Thanks goes to the Federal Ministry of Economics and Energy for their funding of the ZIM projects KK5134113SK1 and KK5446701SK1. Support in model devolepment and programming was enable through founding of the Helmholtz association within the MSE programme, no. 43.31.01. Furthermore, we thank the program 'Mittelbau' funded by the Ministerium of Science, Research and Arts Baden-Württemberg. This work was performed on the computational resource bwUniCluster founded by the Ministry of Science, Research and the Arts Baden-Württemberg and the Universities of the State of Baden-Württemberg, Germany, within the framework program bwHPC.

Data availability statement

The data that support the findings of this study are available from the corresponding author, Leonie Wallat, upon reasonable request.

ORCID

Leonie Wallat http://orcid.org/0000-0002-6434-2005
Michael Selzer http://orcid.org/0000-0002-9756-646X

References

Allen, Samuel M., and John W. Cahn. 1979. "A Microscopic Theory for Antiphase Boundary Motion and Its Application to Antiphase Domain Coarsening." *Acta Metallurgica* 27 (6): 1085–1095. https://doi.org/10.1016/0001-6160(79)90196-2.

Ashby, Mike. 2005. "The Properties of Foams and Lattices." *Philosophical Transactions. Series A, Mathematical, Physical, and Engineering Sciences* 364:15–30. https://doi.org/10.1098/rsta.2005.1678.

Auricchio, Ferdinando, Elena Bonetti, Massimo Carraturo, Dietmar Hömberg, Alessandro Reali, and Elisabetta Rocca. 2020. "A Phase-Field-Based Graded-Material Topology Optimization with Stress Constraint." *Mathematical Models and Methods in Applied Sciences* 30 (8): 1461–1483. https://doi.org/10.1142/S0218202520500281.

Brindley, David, Kishaani Moorthy, Jae-Ho Lee, Chris Mason, Hae-Won Kim, and Ivan Wall. 2011. "Bioprocess Forces and Their Impact on Cell Behavior: Implications for Bone Regeneration Therapy." *Journal of Tissue Engineering* 2011:620247. https://doi.org/10.4061/2011/620247.

Daubner, Simon, Paul W. Hoffrogge, Martin Minar, and Britta Nestler. 2023. "Triple Junction Benchmark for Multiphase-Field and Multi-order Parameter Models." *Computational Materials Science* 219:111995. https://doi.org/10.1016/j.commatsci.2022.111995.

Dong, Guoying, Yunlong Tang, Dawei Li, and Yaoyao Fiona Zhao. 2020. "Design and Optimization of Solid Lattice Hybrid Structures Fabricated by Additive Manufacturing." *Additive Manufacturing* 33:101116. https://doi.org/10.1016/j.addma.2020.101116.

Gao, Jiawen, Baowei Song, and Zhaoyong Mao. 2020. "Combination of the Phase Field Method and BESO Method for Topology Optimization." *Structural and Multidisciplinary Optimization* 61 (1): 225–237. https://doi.org/10.1007/s00158-019-02355-y.

Garcke, Harald, Britta Nestler, and Barbara Stoth. 1999. "A MultiPhase Field Concept: Numerical Simulations of Moving Phase Boundaries and Multiple Junctions." *SIAM Journal on Applied Mathematics* 60 (1): 295–315. https://doi.org/10.1137/S0036139998334895.

Ghabraie, Kazem, Yi Xie, X. Huang, and Gang Ren. 2010. "Shape and Reinforcement Optimization of Underground Tunnels." *Journal of Computational Science and Technology* 4 (1): 51–63. https://doi.org/10.1299/jcst.4.51.

Hötzer, J., A. Reiter, H. Hierl, P. Steinmetz, M. Selzer, and Britta Nestler. 2018. "The Parallel Multi-physics Phase-Field Framework Pace3D." *Journal of Computational Science* 26:1–12. https://doi.org/10.1016/j.jocs.2018.02.011.

Moelans, Nele, Bart Blanpain, and Patrick Wollants. 2008. "An Introduction to Phase-Field Modeling of Microstructure Evolution." *Calphad* 32 (2): 268–294. https://doi.org/10.1016/j.calphad.2007.11.003.

Nestler, Britta, Harald Garcke, and Björn Stinner. 2005. "Multicomponent Alloy Solidification: Phase-Field Modeling and Simulations." *Physical Review E* 71 (4): 041609. https://doi.org/10.1103/PhysRevE.71.041609.

Nestler, Britta, Frank Wendler, Michael Selzer, Björn Stinner, and Harald Garcke. 2008. "Phase-Field Model for Multiphase Systems with Preserved Volume Fractions." *Physical Review E* 78:011604. https://doi.org/10.1103/PhysRevE.78.011604.

Pires, Tiago H. V., John W. C. Dunlop, André P. G. Castro, and Paulo R. Fernandes. 2022. "Wall Shear Stress Analysis and Optimization in Tissue Engineering TPMS Scaffolds." *Materials* 15 (20): 7375. https://doi.org/10.3390/ma15207375.

Reder, Martin, Jana Holland-Cunz, Paula Lorson, Anastasia August, and Britta Nestler. 2023. "Simulative Determination of Effective Mechanical Properties for Digitally Generated Foam Geometries." *Advanced Engineering Materials* 25 (19): 2300340. https://doi.org/10.1002/adem.202300340.

Schoof, Ephraim, Daniel Schneider, Nick Streichhan, Tobias Mittnacht, Michael Selzer, and Britta Nestler. 2018. "Multiphase-Field Modeling of Martensitic Phase Transformation in a Dual-Phase Microstructure." *International Journal of Solids and Structures* 134:181–194. https://doi.org/10.1016/j.ijsolstr.2017.10.032.

Steinbach, Ingo. 2009. "Phase-Field Models in Materials Science." *Modelling and Simulation in Materials Science and Engineering* 17 (7): 073001. https://doi.org/10.1088/0965-0393/17/7/073001.

Sun, Ying, and Christoph Beckermann. 2007. "Sharp Interface Tracking Using the Phase-Field Equation." *Journal of Computational Physics* 220 (2): 626–653. https://doi.org/10.1016/j.jcp.2006.05.025.

Takezawa, Akihiro, Kazuo Yonekura, Yuichiro Koizumi, Xiaopeng Zhang, and Mitsuru Kitamura. 2018. "Isotropic Ti–6Al–4V Lattice via Topology Optimization and Electron-Beam Melting." *Additive Manufacturing* 22:634–642. https://doi.org/10.1016/j.addma.2018.06.008.

Tang, Poh-Soong, and Kuang-Hua Chang. 2001. "Integration of Topology and Shape Optimization for Design of Structural Components." *Structural and Multidisciplinary Optimization* 22 (1): 65–82. https://doi.org/10.1007/PL00013282.

Teimouri, Mohsen, Mahshid Mahbod, and Masoud Asgari. 2021. "Topology-Optimized Hybrid Solid–Lattice Structures for Efficient Mechanical Performance." *Structures* 29:549–560. https://doi.org/10.1016/j.istruc.2020.11.055.

Tung, Cheng-Che, Hsin-Jui Wang, and Po-Yu Chen. 2020. "Lightweight, Compression-Resistant Cellular Structures Inspired from the Infructescence of *Liquidambar Formosana*." *Journal of the Mechanical Behavior of Biomedical Materials* 110:103961. https://doi.org/10.1016/j.jmbbm.2020.103961.

Voigt, W. 1889. "Über Die Beziehung Zwischen Den Beiden Elasticitätsconstanten Isotroper Körper." *Annalen der Physik* 274 (12): 573–587. https://doi.org/10.1002/andp.18892741206.

Wallat, Leonie, Arnd Koeppe, Michael Selzer, Marcus Seiler, Frank Poehler, and Britta Nestler. 2024. "Experimental Evaluation of Phase-Field-Based Load-Specific Shape Optimization of Nature-Inspired Porous Structures." *Materials Today Communications* 38:108088. https://doi.org/10.1016/j.mtcomm.2024.108088.

Wallat, Leonie, Martin Reder, Michael Selzer, Frank Poehler, and Britta Nestler. 2023. "Shape Optimization of Porous Structures by Phase-Field Modeling with Strain Energy Density Reduction." *Materials Today Communications* 37:107018. https://doi.org/10.1016/j.mtcomm.2023.107018.

Wallin, Mathias, and Matti Ristinmaa. 2013. "Howard's Algorithm in a Phase-Field Topology Optimization Approach." *International Journal for Numerical Methods in Engineering* 94 (1): 43–59. https://doi.org/10.1002/nme.4434.

Wang, Yulong, Hirshikesh, Tiantang Yu, Sundararajan Natarajan, and Tinh Quoc Bui. 2024. "Phase-Field Method Combined with Optimality Criteria Approach for Topology Optimization." *Applied Mathematical Modelling* 129:509–521. https://doi.org/10.1016/j.apm.2024.02.006.

Xia, Qi, Tielin Shi, and Liang Xia. 2019. "Stable Hole Nucleation in Level Set Based Topology Optimization by Using the Material Removal Scheme of BESO." *Computer Methods in Applied Mechanics and Engineering* 343:438–452. https://doi.org/10.1016/j.cma.2018.09.002.

Xie, Wenxuan, Qing Xia, Qian Yu, and Yibao Li. 2023. "An Effective Phase Field Method for Topology Optimization without the Curvature Effects." *Computers & Mathematics with Applications* 146:200–212. https://doi.org/10.1016/j.camwa.2023.06.037.

Xue, Xin, Xueqi Chen, Pengfei Zhao, and Cheng Yang. 2023. "Shear Performance of Reinforced Concrete Beams Containing Stirrups with Lower Bend Defects." *Engineering Structures* 280:115718. https://doi.org/10.1016/j.engstruct.2023.115718.

Yeatts, Andrew B., and John P. Fisher. 2011. "Bone Tissue Engineering Bioreactors: Dynamic Culture and the Influence of Shear Stress." *Bone* 48 (2): 171–181. https://doi.org/10.1016/j.bone.2010.09.138.

Zhao, Fei. 2014. "A Nodal Variable ESO (BESO) Method for Structural Topology Optimization." *Finite Elements in Analysis and Design* 86:34–40. https://doi.org/10.1016/j.finel.2014.03.012.